ECS Transactions, 19 (5) 185-199 (2009)
10.1149/1.3119542 ©The Electrochemical Society

Materials Science of Graphene for Novel Device Applications

Geunsik Lee, Cheng Gong, Adam Pirkle, Archana Venugopal, Bongki Lee, SeongYong Park, Laurence Goux, M. Acik, R. Guzman, Yves Chabal, Jiyoung Kim, Eric M. Vogel, Robert M. Wallace, Moon J. Kim, Luigi Colombo,[a] and Kyeongjae Cho*

Department of Materials Science and Engineering, University of Texas at Dallas, Richardson, Texas 75080, USA
[a]Texas Instruments Incorporated, Dallas, Texas 75243, USA
*Email contact: kjcho@utdallas.edu

Realization of graphene based devices will require a controlled integration of graphene into a device structure with multiple material components of metals and insulators. To investigate the fundamental materials problems of graphene devices, a complimentary team of researchers at UTD is applying experimental and theoretical methods to the graphene/metal and graphene/dielectric interface problems. To assess the large area graphene synthesis and the corresponding material properties, graphene oxides and grain boundaries in graphene are also examined by experiments in close connection with modeling study. Through a strong collaborative research in synthesis, characterization, and modeling, we have developed a fundamental understanding of graphene material properties which can facilitate diverse graphene based devices applications.

Introduction

Graphene is a single atomic layer of graphite and has attracted intensive research interests because of technologically promising electronic properties (1). Its electronic structure near the Fermi level is determined by the π-orbital band structure, and has a zero gap at the Dirac point with linear energy-momentum dispersion. The corresponding carrier motion is governed by the Dirac-like effective Hamiltonian with the Fermi velocity as high as 10^6 m/s. The measured mobility is very high (up to 15,000 cm^2/Vs) at 300 K due to ballistic transport (2-4). These unusual electronic properties and potential large area synthesis of graphene have motivated an extensive research on diverse novel device applications including future nanoelectronic devices, novel chemical sensors, spin-resolved transport, pseudo-spin devices, and qubits for quantum computing (5-10).

To realize any graphene based devices, it is necessary to integrate graphene into a functional device structure which has multiple material components such as metals and insulators in direct contact with graphene. Since graphene is extremely thin (one atomic layer), the device properties will strongly depend on the interactions between graphene and other material components. Graphene/metal and graphene/dielectric interfaces are two critical material problems which have not been well understood yet. Another outstanding challenge in graphene based device application is the large area synthesis of graphene without using labor intensive mechanical exfoliation of small size graphene flakes (~ 10 μm). Chemical approaches of graphite oxidation followed by graphene oxide

separation and reduction of graphene oxide provide a promising possibility of large scale production of graphene. However, the reduced graphene oxides are shown to have significant residual oxygen (up to 10 at. %), and further process optimization is necessary to realize the promise of large scale production of high quality graphene using chemical processing. Graphene synthesis on surfaces (Ni, Cu or SiC) is another promising approach to produce large area graphene. A common characteristic of large area graphene is the presence of grain boundaries which may strongly modify the electronic properties of graphene. To investigate these fundamental materials properties, we have organized a complementary research team at the University of Texas at Dallas, and studied metal/graphene interfaces, graphene surface functionalization, graphene oxides and grain boundaries in graphene using experimental and theoretical methods.

In this paper, we will first examine the graphene/metal interface properties using experimental methods (XPS and contact resistance measurement) and compare the measured data with theoretical predictions from quantum mechanical simulations. As an initial part of graphene/dielectric interface study, we will show the effect of ozone treatment on the atomic layer deposition (ALD) growth of Al_2O_3 layer on top of the chemically inert highly ordered pyrolytic graphite (HOPG) surface. The results are explained by the *ab initio* simulation of ozone interaction with graphene surface. Using IR spectroscopy, diverse atomic structure of graphene oxides are investigated, and the characteristic frequencies are compared with the calculated C-O-C frequencies. SEM and HRTEM are used to identify the grain boundaries (GBs) in graphene, and the electronic properties of GBs are studied using quantum transport simulations.

Experimental Study of Graphene Material Properties

We will first discuss four complementary experimental studies of graphene material properties: graphene/metal, graphene/dielectric, graphene oxide, and GBs in graphene. As we have discussed, the graphene/metal and graphene/dielectric interface studies are motivated to develop an optimized metal contact and gate dielectric for graphene electronic devices. Studies on graphene oxides and GBs are motivated by the large area graphene synthesis and the corresponding materials properties. In this experimental section, we will report the recent findings on these four aspects of graphene material properties, and each of the experimental findings will be compared with the modeling analysis in the following theoretical section.

Metal/Graphene Interface

To investigate the chemical and electronic properties of graphene/metal interfaces, we have used a combination of x-ray photoelectron spectroscopy (XPS) and contact resistance measurements. Due to the large analysis spot size of XPS, the interface of various contact metals (Al, Pt, Ti, Ni, Hf) on graphite was studiedwith the assumption that the surface reactions detected on well ordered graphite are similar to few-layer graphene surfaces. These studies were carried out in an *in-situ* ultrahigh vacuum (UHV) cluster system which includes deposition, annealing and analysis modules as described previously (11). Thin metal films were deposited by e-beam evaporation and annealed under UHV at 500°C for 10 minutes. XPS data are collected immediately after deposition and after annealing. The impact of an additional UHV anneal at 500°C prior to deposition,

intended to remove physisorbed species such as H_2O and organics, has also been examined. Our studies indicate that initial surface condition and subsequent process impacts interface bonding following metal depositions.

In Figures 1 and 2, we show XPS analyses for Ni and Pt, repectively. In case of Pt, the C 1*s* intensity increases and Pt 4*f* decreases. This suggests the formation of Pt clusters, partially exposing the underlying graphite (increase in C 1*s* signal) and causing attenuation of Pt 4*f* photoelectrons (decrease in Pt 4*f* signal). Our atomic force microscopy (AFM) data, shown in Figure 3, confirms this morphology. The clusters appear to be 30 to 50 nm wide and 5 to 10 nm high. It is noted that the Ni/graphene XPS data shows a very small side peak corresponding to Ni-C bond formation whereas Pt/graphite XPS data do not show similar side peak. The nature of interface chemistry will be further discussed in comparison with the Ni/graphene and Pt/graphene interface modeling using the density functional theory (DFT) method.

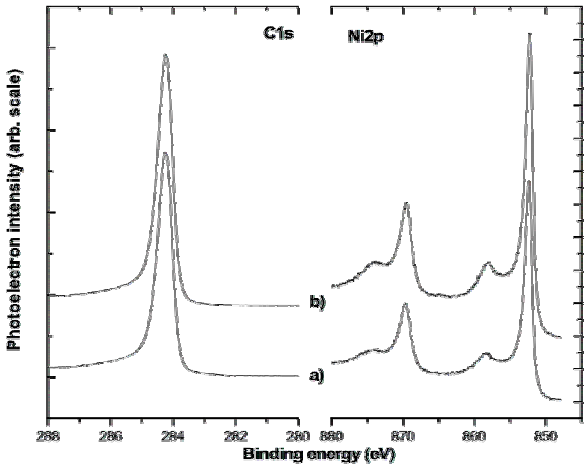

Figure 1. XPS analysis of 1 nm Ni on HOPG, a) immediately after Ni deposition, b) after 500 °C/10 min vacuum anneal with *in-situ* surface clean

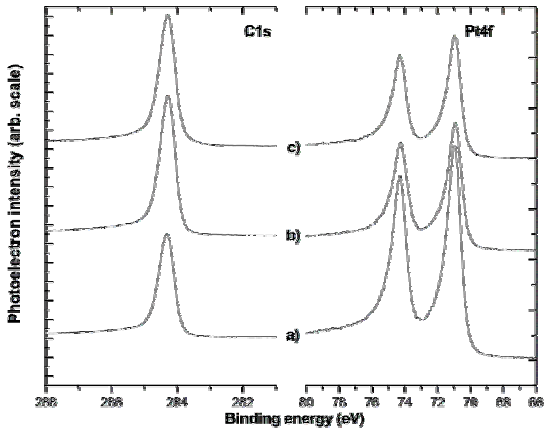

Figure 2. XPS analysis of 1 nm Pt on HOPG, a) immediately after Pt deposition, b) after 500 °C/10 min vacuum anneal with in-situ surface clean, and c) after 500 °C/10m min vacuum anneal without *in-situ* surface clean.

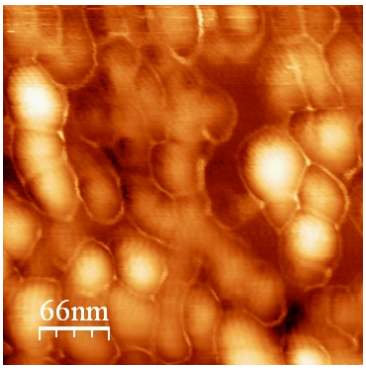

Figure 3. Tapping mode AFM image of Pt on HOPG surface.

For a ballistic conductor like graphene, one of the major factors limiting device scalability will be contact resistance, as similar studies on carbon nanotubes indicate (12). Although there has been significant progress in graphene based devices, there have been few studies of factors such as metal type, metal workfunction and number of layers in the graphene stack on metal/graphene contact resistance. Transfer length measurements using large area contacts (~10^{-4} cm^2) on HOPG have been performed on a variety of metals (Figure 4). The total resistance as a function of distance between contacts is shown in Figure 4. The total resistance is independent of distance indicating that the total resistance is dominated by contact resistance. The contact resistance is also observed to be similar for a wide variety of metals although the metal workfunction varies from 4.3 eV to 5.6 eV. This is likely due to the limited interaction/bonding between the metal and HOPG. Similar measurements are being performed on single- and few-layer sheets of graphene. Their resistances are found to be two orders of magnitude higher than those on HOPG. These contact resistance data are consistent with the XPS data which show negligible chemical interaction at the graphene/metal interface. The significance of interface chemistry on the contact resistance will be discussed in the modeling section.

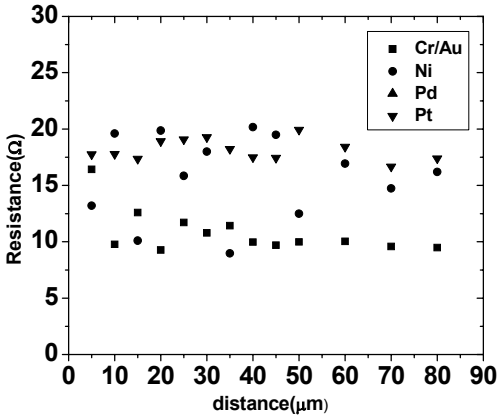

Figure 4. Transfer length measurements for metal contacts on HOPG.

Gate Dielectric Growth on Graphene

Most graphene device experiments have so far been performed using a single back gate structure typically with a blanket SiO_2 layer on top of a degenerately doped Si wafer.

However, this structure cannot provide a localized field essential for surface channel field effect transistors (FET) applications. To make use of top-gated devices, one of the most critical obstacles is the absence of a high quality gate dielectric on top of the graphene surface. This is because the chemically inert nature of the graphene basal planes inhibits the deposition of high quality and uniform gate dielectric films. In this study, we present the characteristics of dielectrics employed by atomic layer deposition on top of a highly oriented pyrolytic graphite (HOPG) surface for localized gate applications.

Fig. 5(a) shows an AFM image of Al_2O_3 layer deposited from TMA/H_2O on top of the HOPG surface. The image shows that the Al_2O_3 layer (200 cycles) from TMA/H_2O on the fresh HOPG surface exhibited selective deposition only on atomic step edges as shown as stripes in Fig. 5(a). No deposition occurred on basal planes due to a chemical inertness of the surface. This selective deposition is ascribed to the chemical reactivity of step edges caused by broken dangling bonds. This result shows that the conventional H_2O process for ALD-oxide produces a preferential growth of Al_2O_3 layer, which is not desirable for top-gated graphene devices.

By utilizing an O_3 treatment on the HOPG surface prior to ALD deposition, it was found that Al_2O_3 layer was conformally deposited along the atomic step edges as well as on the basal planes of the HOPG surface, with a small root mean square (RMS) roughness value of ~0.2 nm, as shown in Fig. 5(b). This result suggests that O_3 pretreatment renders the chemically inert HOPG surface reactive towards ALD precursors, which leads to the desirable two-dimensional growth mode during Al_2O_3 deposition from TMA/O_3. The effect of ozone on graphene and the mechanisms of producing chemical active sites on graphene basal plane are discussed in the modeling section.

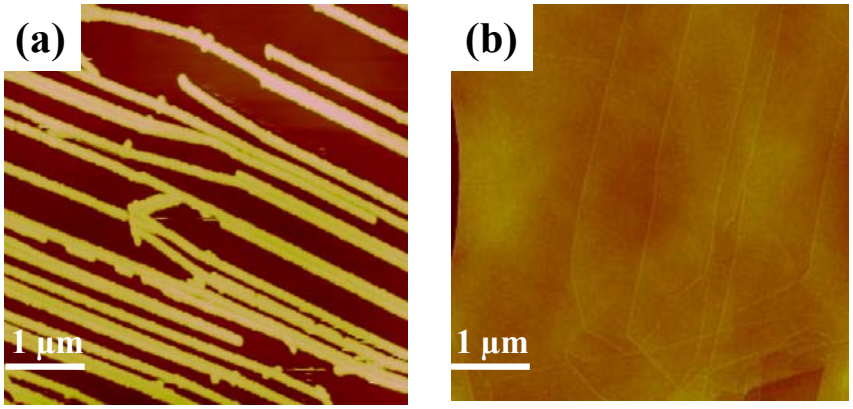

Figure 5. (Color) (a) AFM image of the sample with Al_2O_3 layer deposited from TMA/H_2O process (200 cycles) at 200°C on HOPG. (b) Al_2O_3 layer from TMA/O_3 process (50 cycles) on the ozone-treated HOPG surface at 200°C.

IR Study of Graphene Oxide

We have examined graphite oxide reduction as a potential method for graphene synthesis (14, 15). The reduced graphene oxide is known to have a significantly reduced mobility and residual oxygen groups. To understand the atomic structures of such residual oxygen, we have studied the IR spectra of graphene oxides under thermal

annealing. Using IR spectroscopy and Raman characterization, we have investigated graphite oxide (GO) synthesis and reduction. Graphite oxide synthesis combines Kovtyukhova, *et. al* and Hummer *et. al* methods for the oxidation steps (16,17).

Graphite powder, purchased from Bay Carbon Inc. in SP-1 grade, was used as a starting material. Before the oxidation step, a pretreatment step was performed according to Kaner *et. al* method (18). Graphite powder (6g) was introduced into a hot (80°C) concentrated H_2SO_4 (25 ml) solution including $K_2S_2O_8$ (5g) and P_2O_5 (5g) additions successively. This mixture was stirred for 4.5 hours at 80°C to dissolve all the components and then diluted to 1L with DI water. After keeping overnight, it was filtered using a 0.2 micron Nylon Millipore filter and washed thoroughly with approximately 500 ml DI water to remove all the traces of acid solution. Next, the solid was dried on a watch glass overnight. For oxidation of graphite powder, acid-treated graphite powder was added to a bath of 230 ml H_2SO_4 held at 0°C. Potassium permanganate ($KMnO_4$), (30g), was then added slowly to H_2SO_4 and stirred to dissolve in the acid mixture by keeping the temperature at 10°C. The reaction was kept at 35°C and 460 ml of DI water was introduced slowly after 2 hours and while stirring the solution continuously for 2 hours by successive dilution with 1.4 ml DI water. Lastly, 30% of H_2O_2 solution was added and a yellow solid of graphite oxide was obtained after being centrifuged and washed with a 2.5L of aqueous 10 % HCl solution and with a 2.5 L of DI water. The yellow solid was dried in air and a dark brown solution was prepared by dispersion in water (2% w/w). The solution was washed with DI water several times for purification and centrifuged at 10000 rpm for 20 minutes each time to remove the impurities, such as sulfate ions. To remove any other metal contaminant, a dialysis step was done in a regenerated cellulose membrane (Spectra/Por Float-A-Lyzer, Biotech, Spectrum Laboratories, Inc.) for 2 weeks in DI water (refreshed every day) within a 1L beaker by constant stirring at 200 rpm.

The resulting graphene oxide flakes, obtained by drying the solution on various substrates, were studied using FTIR spectroscopy. In particular, the thermal reduction of graphene oxide in vacuum was monitored by transmission IR spectroscopy up to 500°C in a high temperature cell (19). In the first trial, the sample was heated to 60°C, 80°C, 120°C, 160°C, 180°C and 200°C, and 500°C in the second trial. The reference and the measurements were taken at 60°C for each temperature after annealing. Figures 6 and 7 summarize the FTIR results with stacked differential spectra of thermal annealing of GO. The partial loss of water molecules can be seen with a broad peak in the range of 3200 cm^{-1} to 3600 cm^{-1} at 100°C (Figure 7). The disappearance of hydroxyl groups was observed at 300°C as shown in Figure 7. Formation of CO_2 is observed at 100°C (Figure 7) and gradually increases as the sample is heated to 160°C. There is clear evidence of the formation of sp^2 hybridized C=C at 1520 cm^{-1}. The peak at 1730 cm^{-1}, which is attributed to carboxyl groups at the edges of GO is also observed. In addition, peaks at 1330 cm^{-1} (C-O-C) and 1227 cm^{-1} (C-O) correspond to the epoxy or peroxide groups on the rough surface of GO (Figure 6). As the sample is heated up, initially there is an increase of the epoxy or peroxide groups, followed by a decrease above 180°C (Figure 6). Overall, Figure 7 indicates that GO becomes more conductive as the annealing temperature is increased up to 500°C as exhibited by the increase in the absorbance of the peaks. However, even after 500°C annealing, there is still oxygen remaining in the form

of epoxy and peroxide. The specific characteristics of the epoxy at 1330 cm^{-1} (will be compared with the modeling data.

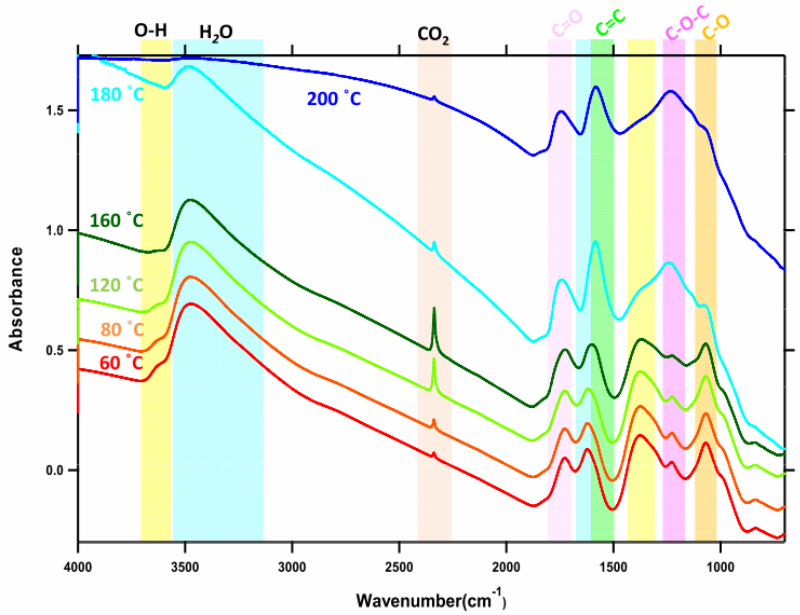

Figure 6. (Color) Transmission IR absorbance as a function of thermal annealing at 60°C (red), 80°C (orange), 120°C (green), 160°C (dark green), 180°C (blue) and 200°C (dark blue) within gradual increments showing the formation of carboxyl, epoxy or peroxide groups and removal of water molecules.

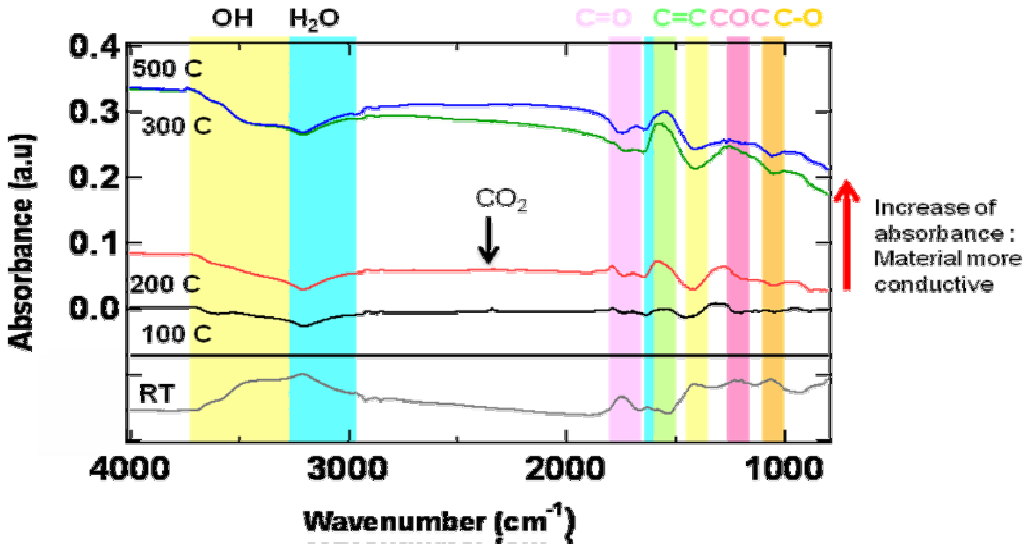

Figure 7. **(**Color**)** Differential IR absorbance spectra (each spectrum referenced to that of the previous treatment) of GO at room temperature (gray) (ref. to clean Si), and after annealing to 100°C (black), 200°C (red), 300°C (green) and 500°C (blue) showing increase in conductivity due to increase of absorbance at high temperatures.

Grain Boundaries in HOPG

LEED experiments on HOPG and natural graphite have shown that the HOPG has multiple crystalline domains with different relative orientations compared to natural graphite which shows a single crystalline domain. To examine detailed atomic structures of the grain boundaries separating crystalline domains, we have performed SEM and HRTEM study of HOPG. HOPG from Structure Probe, Inc. (Grade SPI-1) was used for our experiments. The graphite surface was cleaned by removing the top surface with scotch tape in order to have a freshly "cleaved" surface without damage or significant contamination. A Ga ion beam induced secondary electron image by dual beam FIB/SEM (FEI NOVA 200) with an acceleration voltage of 30kV was acquired to delineate the grain structure of graphite, since high energy ion bombardment enhances the channeling contrast between different crystal orientations. The image shown in Figure 8(a) reveals that grains have an average size of 30 μm. Figure 8(b) shows the high resolution transmission electron microscopy (HRTEM) image for the same sample. The electronic structure of a similar grain boundary is discussed in the modeling section.

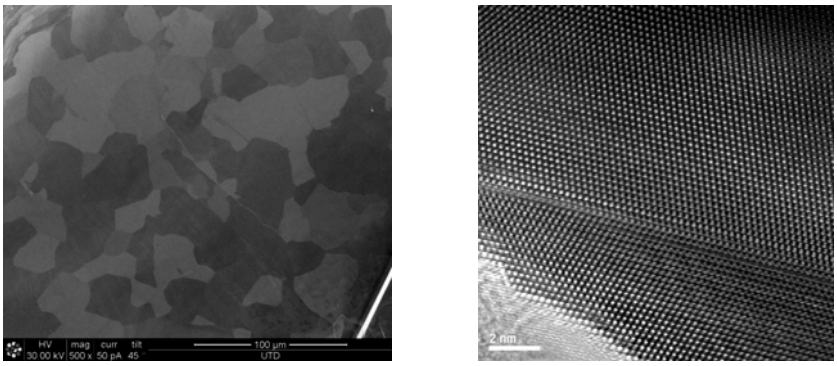

(a) (b)

Figure 8. (a) Ga ion beam-induced secondary electron image by dual bream FIB/SEM is shown. Different brightness represents individual grain in HOPG which has different crystal orientations. The scale bar is 100 micron. (b) HRTEM image of the sample used in (a). The scale bar is 2 nm.

Theoretical Study of Graphene Material Properties

In this section, we will discuss the modeling study of four graphene materials properties investigated in the experimental section. The electronic structures of Ni/graphene and Pt/graphene have been studied using the DFT method. The ozone molecule interaction with graphene basal plane is studied to explain the observed effect of ozone pretreatment on the ALD growth of alumina. The vibration frequencies of epoxide groups on graphene basal plane are calculated and compared with the experimental IR spectroscopy data. The electronic structures of a grain boundary in graphene and graphene nanoribbon are calculated to assess the effects of grain boundary on the graphene based device performance. For the DFT electronic structure calculations, we have used the Vienna ab initio simulation package (VASP) with its projected augmented wave pseudopotentials within the local density approximation (LDA) scheme (20-22). To study the effect of grain boundary on the charge transport in graphene, we

have used quantum transport simulations based on nonequilibrium Green's function (NEGF) formalism (23, 24).

Electronic Structure of metal/Graphene Interfaces

The interaction between Ni or Pt metal layer and graphene was modeled and compared with the experimental data. To model the interfaces, we have used three atomic layers of (111) face-centered cubic crystalline metal surface and 10 Å vacuum region. For the Ni/graphene interface, the lattice mismatch is 1.2 % relative to graphene, and we used 1x1 unit cell of graphene with compressed metal surface. For Pt, the lattice mismatch is 12.7 % which is too large to use 1x1 unit cell so that we have used 2x2 graphene unit cells which accommodate three Pt atoms with −2.4 % mismatch. After optimizing the interface structures, we have calculated the band structures to examine how the intrinsic π band structure of graphene is changed by the metal layers. For that purpose, we project the C-π orbital's contribution on each state of the obtained band structure.

To study the interface bonding strength, the total energies are calculated by varying the normal distance between the graphene sheet and the metal layer. For Ni, three different interface atomic geometries (top, bridge and hexagon center) are examined, and the two geometries (top and bridge) have strong interface bonding with the normal distance of about 2.0 Å. The hexagon center geometry bonds weakly at the distance of 3.3 Å. For Pt, we find only weakly bonded interface with the normal distance of 3.3 Å. In the XPS measurements on the interface of metal (Pt, Ni) and HOPG (Figures 1 and 2), it was shown that Ni/HOPG interface shows a small side peak corresponding to Ni-C bonding whereas no carbide bond signal were detected for Pt/graphene. However, the contact resistance measurement has shown similar behavior for Ni and Pt on graphene. To understand the experimental data, we have examined the electronic structures of metal/graphene interfaces.

In Figure 9(a), we show calculated band structures for the Ni layer on graphene for strong (top) and weak (center) interface bonding. When Ni atoms interact strongly with graphene for the top and bridge interface geometries, the π band structure of pure graphene is significantly changed by pushing the valence π band down below Ni-*d* bands. On the other hand, the conduction band of graphene is only slightly modified by the metal-graphene interaction. At the strongly interacting Ni/graphene interface, the C-π orbitals and Ni-*d* orbitals hybridize to form π band structure with a gap and the localized Ni-*d* bands near the Fermi level within the π band gap. In contrast, the interface electronic structure with weak bonding (center) shows a superposition of graphene and Ni metal surface band structures indicating negligible interaction between Ni surface and graphene. For this weak interface, the Fermi level shift is negligible indicating negligible charge transfer between the metal and graphene. These Ni/graphene interface electronic structures will remain in the Ni/graphite interface used in the experimental studies in Figs. 1 and 2. The electronic band structure of graphite shows a weak interlayer C-π orbital interaction, but they are much weaker than the Ni-C interaction shown in Fig. 9(a).

Figure 9(b) shows the calculated band structure for Pt/graphene, and more bands are shown since 2x2 band structure is unfolded into 1x1 Brillouin zone. This band structure

is similar to the weakly interacting Ni/graphene, but there is a difference in the Fermi level shift. Compared to pure graphene, there is a small upward shift of the Fermi level (0.17 eV) indicating small amount of electron transfer from graphene to Pt. This is consistent with the fact that the work function of Pt (6.0 eV) is higher than that of graphene (4.6 eV).

The XPS experiment has shown an indication of metal-carbon bonds formed at the Ni/graphene interface consistent with the electronic structure analysis in Fig. 9(a). However, the contact resistance measurement has shown high resistance for both Ni/graphene and Pt/graphene interfaces even though their interface electronic structures are quite different as shown in Fig. 9 (a) and (b). There are two different mechanisms to increase the contact resistance for the metal/graphene interface. For strongly interacting Ni/graphene interface, the metal d-bands are within the π band gap leading to charge injection barrier. On the other hand, for weakly interaction interface, the electron transport goes through a tunneling barrier at the metal-graphene interface leading to high contact resistance. This result seems to be consistent with the study on transition metal (TM) and carbon nanotube (CNT) contact resistance which shows that the late TM elements like Ni and Pt tend to form weak bonds with CNT exhibiting high contact resistance (25). However, more studies are necessary to clarify the relationship between the bond character and the contact resistance for metal-graphene interfaces.

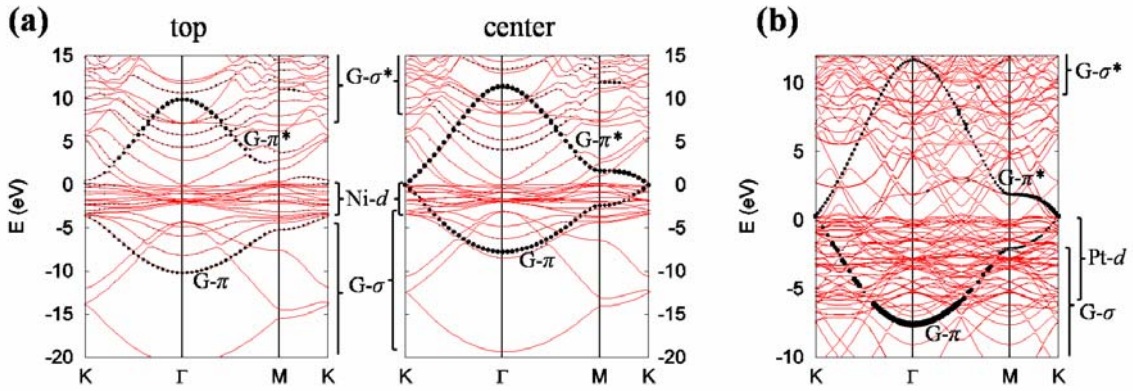

Figure 9. Band structures for (a) Ni/graphene and (b) Pt/graphene interfaces. The black dots represent C-π orbital contribution, and its bonding and anti-bonding bands are indicated by G-π and G-π* respectively. The sp^2 σ and σ* bands of graphene are also indicated together with metal *d* bands. The 2x2 unit cell BZ of Pt/graphene is unfolded into 1x1 BZ. The Ni surface has a strong or weak interaction with graphene depending on the lateral position of Ni surface atoms. The top and bridge positions form strong bonding, and their band structures are almost the same (only the top is shown). The center Ni position forms weak bonding and preserves pure graphene band structure. The Pt layer forms only weak bonding, and graphene π and π* bands are clearly shown by black dots in (b).

Ozone Adsorption on Graphene

The experimental study of ALD growth on graphite has shown that the ozone pre-treatment on graphite facilitate a uniform alumina growth on the basal plane. This experimental result strongly indicates that the ozone treatment creates hydrophilic reaction sites on graphene basal plane which can initiate the subsequent uniform growth of alumina during TMA/O_3 cycles. To investigate the identity of such reaction sites induced by ozone treatment, we have modeled an ozone molecule interaction with graphene basal plane using the DFT method. We have used a model with 3x3 periodic unit cell of graphene with an ozone molecule, and the resulting ozone-ozone image distance is 7.38 Å. This cell size is not large enough for absolute convergence, but the adsorbate interaction remains constant and can be ignored when we compare the total energies calculated within the same unit cell. The vertical unit cell size is chosen to be 15 Å. The k-grid of 5×5×1 is adopted for the Brillouin zone integration. The spin polarization within LSDA scheme is included to obtain accurate ground state energy.

As shown in Figure 10(a), we calculated the total energy by changing the height (h) between the graphene sheet and the lower O atoms of an ozone molecule. At h = 2.9 Å, ozone has a weak bonding with graphene, which is a physisorption state. However, at h = 1.5 Å, the ozone molecule dissociates and forms one stable epoxide and a separated oxygen molecule, as shown in Figure 10(b). This dissociated state has 0.06 eV lower energy than the physisorption state. The oxygen molecule will move away from the surface and the remaining epoxide group will form the hydrophilic reaction sites. This result could explain the experimental finding that ozone pretreatment enables conformal Al_2O_3 growth by ALD.

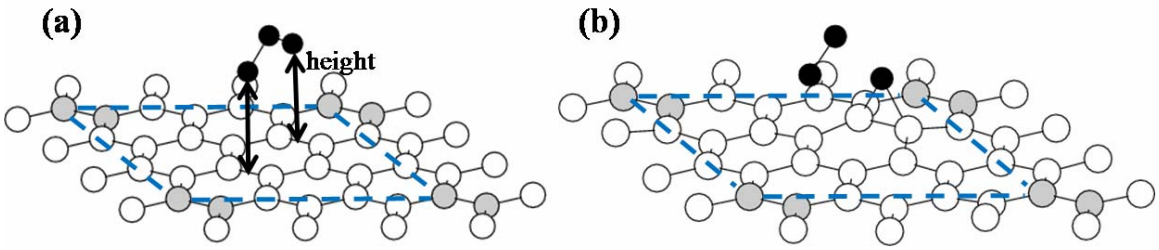

Figure 10. (a) A theoretical model for ozone adsorption onto graphene is shown. The ozone molecule interaction with graphene is calculated by varying the height, indicated by the arrow. (b) The dissociated adsorption of ozone at the height h = 1.5 Å is shown. One epoxide group is formed on graphene basal plane and an oxygen molecule is also shown.

Vibration Frequencies of Oxidized Graphene

In the experimental section, we have studied the graphite oxides and their IR spectra under thermal annealing condition. From the IR spectra, epoxy (C-O-C) and peroxide (C-O) peaks are shown to persist up to 500°C annealing. The peroxide peaks are originating from the edge oxide bonding at graphene edges at the outer boundaries and inner boundaries of etched out sections. The epoxy peaks are originating from the epoxide group formed on graphene basal plane whose structure was shown in Fig. 10(b). To

validate this assignment of epoxy peaks, we have performed DFT study of vibration frequencies of epoxide on graphene basal plane. We have used the frozen phonon approximation, in which we calculate the total energies by displacing an oxygen atom along the normal mode direction. We have considered two types of oxidation group, as shown in Figure 11, strained epoxide group and relaxed C-O-C group with broken C-C bond. For each structure, the normal modes we consider are asymmetrical (parallel to graphene plane) and symmetrical (normal to graphene plane) motions of the chemisorbed oxygen atoms. We have checked the convergence of the calculated vibration frequency, and the energy cutoff of 400 eV was high enough to give a converged value within 10~20 cm^{-1} accuracy. For a test, we have calculated the stretching frequency of an isolated CO molecule and obtained 2175 (± 20) cm^{-1} which agrees well with the experimental value 2143 cm^{-1}.

For the strained epoxide group (left in Figure 11), frequencies for the asymmetrical and symmetrical modes are calculated to be 601 and 863 cm^{-1}, respectively. For the relaxed C-O-C group (shown in the right side of Figure 11), the calculated frequencies are 1310 and 442 cm^{-1} for the asymmetrical and symmetrical modes. By comparing these data with the IR experiment shown in Figure 7, we can assign the peak at 1330 cm^{-1} to the asymmetrical mode vibration of relaxed C-O-C group. This comparison shows that the graphene oxide has significant structural change due to oxidation by breaking the C-C bond from the strained epoxide group to relaxed C-O-C group. However, the presence of strained expoxide group is difficult to confirm due to an experimental difficulty in measuring the lower frequency IR peaks below 1000 cm^{-1}.

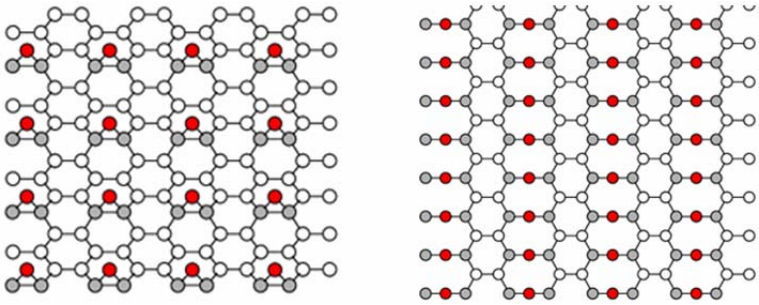

Figure 11. Theoretical models used for the calculation of vibration frequencies of oxygen atoms adsorbed on graphene in forms of (left) strained epoxide group (right) relaxed C-O-C group. In both, white and gray circles mean carbon atoms, and red circles represent oxygen atoms.

Electronic Transport across Grain Boundaries

The SEM and HRTEM images in the experimental section have shown the grain boundaries in HOPG (Figure 8), and they can modify the electronic properties of graphene. To examine the detailed nature of grain boundary effects, we have calculated the electronic structure and electrical conductance across the boundary using NEGF formulism (23, 24). The Hamiltonian is described within the nearest-neighbor (NN) π orbital tight-binding approximation. The NN coupling parameter is taken to be $t_{ij} = -2.77$ eV which is shown to reproduce the DFT band structure of graphene. We consider a large

angle GB formed by heptagon-pentagon row as shown in Figure 12(a), and focus the modeling study on the effect of GB on electronic transport. For this purpose, we calculate the conductance of an ideal graphene without GB and compare it with the GB results. We have considered a finite width nanoribbon (W=1.8 nm) as shown in Figure 12(a).

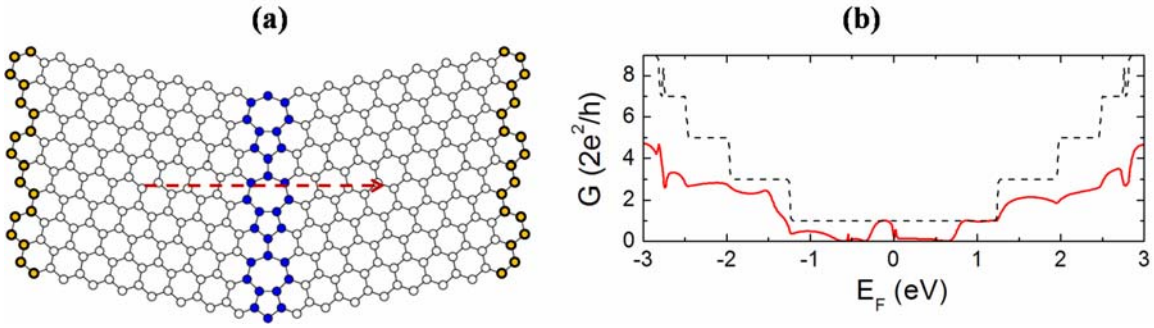

Figure 12. (Color) (a) The graphene channel with a grain boundary (GB) is shown. The C atoms in the vertical heptagon-pentagon row as GB are indicated by the dark filled (blue) circle. The source (left) and drain (right) electrode C atoms to which the semi-infinite boundary condition is applied are indicated by the gray (orange) circle. The arrow indicates the transport direction of electrons. (b) Simulated conductance by NEGF formulism for the nanoribbon in (a) are shown together with the conductance for the ideal case without GB (dashed line).

The calculated conductance as a function of the Fermi level of the channel is shown in Figure 12(b). The conductance is substantially suppressed by the grain boundary. We confirmed that the state corresponding to the peak at E_F = –0.1 eV in Fig. 12(b) is delocalized along the ribbon edge. However, most states related to the diminishing conductance near E_F = 0.0 eV, are strongly localized at pentagons and heptagons. In the case of an ideal ribbon, those states are delocalized over the whole ribbon, leading to unit conductance at $|E_F| \leq 1.25$ eV These results show that the grain boundary in graphene nanoribbons does not have a strong influence on the edge states transport, but significantly suppresses the conductance at other energy range.

Conclusions

In this paper, we have examined the metal/graphene interface, oxide growth on graphene basal plane, atomic structure graphene oxide, and grain boundaries in graphene using experimental and modeling approaches. The complementary study has elucidated the nature of metal/graphene interface electronic structure explaining the origin of subtle Ni-C peaks in the XPS data and provided likely origins of large contact resistance measured in transfer length experiment. Experimental demonstration of ozone effect on ALD growth on the graphene basal plane is explained by the detailed modeling study of epoxide group formation by chemisorptions of ozone on the graphene basal plane. The IR spectroscopy peak of epoxy (C-O-C) peak was shown to be stable under high temperature annealing and the same peak was identified in DFT modeling as the relaxed C-O-C epoxide group in which the initial C-C bond in broken by the oxygen insertion.

This comparative study has provided an insight on detailed atomic structure of graphene oxides and origin of the thermal stability. Grain boundaries are experimentally identified by SEM and HRTEM studies, and their electronic properties are examined by the quantum transport modeling. The calculated conductance shows that the GB decreases the overall conductance significantly except for the one through the edge states. These four graphene material case studies illustrate the importance of the detailed materials understanding to optimize the graphene based device structures. Further details of these research results will be published elsewhere.

Acknowledgments

This work is sponsored by the Nanoelectronic Research Initiative (NRI SWAN Center - #2006-NE-1464)

References

1. A. K. Geim and K. S. Novoselov, *Nature Mater.*, **6**, 183 (2007).
2. K. S. Novoselov, A. K. Geim, S. V. Morozov, D. Jiang, Y. Zhang, S. V. Dubonos, I. V. Grigorieva, and A. A. Firsov, *Science*, **306**, 666 (2004).
3. Y. Zhang, Y.-W. Tan, H. L. Stormer, and P. Kim, *Nature*, **438**, 201 (2005).
4. C. Berger et al., *Science*, **312**, 1191 (2006).
5. M. C. Lemme, T. J. Echtermeyer, M. Baus, and H. Kurz, *IEEE Electron Device Lett.*, **28**, 282 (2007).
6. J. R. Williams, L. DiCarlo, and C. M. Marcus, *Science*, **317**, 638 (2007).
7. F. Schedin, A. K. Geim, S. V. Morozov, E. W. Hill, P. Blake, M. I. Katsnelson, and K. S. Novoselov, *Nature Mater.*, **6**, 652 (2007).
8. Y.-W. Son, M. L. Cohen, and S. G. Louie, *Nature*, **444**, 347 (2006).
9. H. Min, R. Bistritzer, J-J Su, and A. H. MacDonald, *Phys. Rev. B*, **78**, 121401(R) (2008).
10. B. Trauzettel, D. V. Bulaev, D. Loss, and G. Burkard, *Nature Phys.*, **3**, 192 (2007).
11. R. M. Wallace, *Electrochem. Soc. Trans.*, **16**, 255 (2008).
12. J. Tersoff, *Appl. Phys. Lett.*, **74**, 2122 (1999).
13. C. Thomsen and S. Reich, *Phys. Rev. Lett.*, **85**, 5214 (2000).
14. C. G. Navarro, R. T. Weitz, A. M. Bittner, M. Scolari, A. Mews, M. Burghard, and K. Kern, *Nano Lett.*, **7**, 3499 (2007).
15. S. Stankovich, D. A. Dikin, R. D. Piner, K. A. Kohlhaas, A. Kleinhammes, Y. Jia, Y. Wu, S. T. Nguyen, and R. S. Ruo , *Carbon*, **45**, 1558 (2007).
16. N. I. Kovtyukhova, P. J. Ollivier, B. R. Martin, T. E. Mallouk, S. A. Chizhik, E. V. Buzaneva, and A. D. Gorchinskiy, *Chem. Mater.*, **11**, 771 (1999).
17. W. S. Hummers Jr. and R. E. Offeman, *J. Am. Chem. Soc.*, **80**, 1339 (1958).
18. S. Gilje, S. Han, M. Wang, K. L. Wang, and R. B. Kaner, *Nano Lett.*, **7**, 3394, (2007).
19. I. Jung, M. Vaupel, M. Pelton, R. Piner, D. A. Dikin, S. Stankovich, J. An, and R. S. Ruoff, *J. Phys. Chem. C*, **112**, 8499 (2008).
20. G. Kresse and J. Hafner, *Phys. Rev. B*, **47**, 558 (1993); G. Kresse and J. Fürthmuller, *Phys. Rev. B*, **54**, 11169 (1996).
21. P. E. Blöchl, *Phys. Rev. B*, **50**, 17953 (1994); G. Kresse and J. Joubert, *Phys. Rev. B*, **59**, 1758 (1999).

22. D. M. Ceperley and B. J. Alder, *Phys. Rev. Lett.*, **45**, 566 (1980).
23. A. Svizhenko, M. P. Anantram, T. R. Govindan, B. Biegel, and R. Venugopal, *J. Appl. Phys.*, **91**, 2343 (2002).
24. S. Datta, *Electronic Transport in Mesoscopic Systems*, Cambridge University Press, Cambridge, UK, (1995); S. Datta, *Quantum Transport: Atom to Transistor*, Cambridge University Press, Cambridge, UK, (2005).
25. A. N. Andriotis, M. Menon, and G. E. Froudakis, *Appl. Phys. Lett.*, **76**, 3890 (2000).
26. J. Andzelm, N. Govind, and A. Maiti, *Chem. Phys. Lett.*, **421**, 58 (2006).